Contrails to Cirrus—Morphology, Microphysics, and Radiative Properties

DAVID ATLAS

Laboratory for Atmospheres, NASA Goddard Space Flight Center, Greenbelt, Maryland

ZHIEN WANG*

Goddard Earth Science and Technology Center, University of Maryland, Baltimore County, Baltimore, and NASA Goddard Space Flight Center, Greenbelt, Maryland

DAVID P. DUDA

National Institute of Aerospace, NASA Langley Research Center, Hampton, Virginia

(Manuscript received 27 December 2004, in final form 30 June 2005)

ABSTRACT

This work is two pronged, discussing 1) the morphology of contrails and their transition to cirrus uncinus, and 2) their microphysical and radiative properties. It is based upon the fortuitous occurrence of an unusual set of essentially parallel contrails and the unanticipated availability of nearly simultaneous observations by photography, satellite, automated ground-based lidar, and a newly available database of aircraft flight tracks. The contrails, oriented from the northeast to southwest, are carried to the southeast with a component of the wind so that they are spread from the northwest to southeast. Convective turrets form along each contrail to form the cirrus uncinus with fallstreaks of ice crystals that are oriented essentially normal to the contrail length. Each contrail is observed sequentially by the lidar and tracked backward to the time and position of the originating aircraft track with the appropriate component of the wind. The correlation coefficient between predicted and actual time of arrival at the lidar is 0.99, so that one may identify both visually and satellite-observed contrails exactly. Contrails generated earlier in the westernmost flight corridor occasionally arrive simultaneously with those formed later closer to the lidar to produce broader cirrus fallstreaks and overlapping contrails on the satellite image. The minimum age of a contrail is >2 h and corresponds to the longest time of travel to the lidar. The lag between the initial formation of the contrail and its first detectability by Moderate-Resolution Imaging Spectroradiometer (MODIS) is ≈33 min, thus accounting for the distance between the aircraft track and the first detectable contrail by satellite. The lidar also provides particle fall speeds and estimated sizes, optical extinction coefficients, optical thickness (τ = 0.35), and ice water path (IWP = 8.1 g m^{-2}). These values correspond to the lower range of those found for midlatitude cirrus by Heymsfield et al. The ice water per meter of length along the cloud lines is 10^3–10^4 times that released by typical jet aircraft. The synthesis of these findings with those of prior investigators provides confidence in the present results. Various authors find that contrail-generated cirrus such as reported here contribute to net regional warming.

1. Introduction

The observation of the transformation of aircraft contrails to cirrus clouds has been reported repeatedly over the last half-century. Appleman (1953) was one of the first to determine the atmospheric conditions in which ice crystals would form and persist. Knollenberg (1972) made the earliest in situ microphysical measurements in the resulting cirrus uncinus clouds. Further microphysical studies were made by Heymsfield (1975), and again many years later (Heymsfield et al. 1998). Konrad and Howard (1974) provided an insightful morphology of contrail cirrus and fallstreaks as viewed by ultrasensitive radars.

A number of investigators have reported the origin and growth of the initial tufts associated with contrails

* Current affiliation: Department of Atmospheric Sciences, University of Wyoming, Laramie, Wyoming.

Corresponding author address: Dr. David Atlas, Distinguished Visiting Scientist, 3116 Gracefield Rd. (#322), Silver Spring, MD 20904.
E-mail: davnlu@comcast.net

(Lewellen and Lewellen 2001; Gierens 1996) while Schröder et al. (2000) measured their initial microphysical properties during their transition to cirrus.

The reader will also find a number of useful papers on the subject in a special issue of *Geophysical Research Letters* (1998, Vol. 25, No. 9) dealing with the program "The Subsonic Aircraft: Contrail and Cloud Effects Special Study (SUCCESS)" (e.g., Minnis et al. 1998; Spinhirne et al. 1998; Lawson et al. 1998; Uthe et al. 1998). A particularly enlightening study of the spreading and growth of contrail clouds has resulted from the numerical simulations of Jensen et al. (1998). Recent interest in contrails has focused upon their climatic impact and their geographical distribution (Minnis et al. 2004; DeGrand et al. 2000). All of the above provide the background for the present study. The reader is referred to a fine review article by Minnis (2003) for further background.

It was the exciting view of the transformation of a series of contrails seen by the lead author and the fortuitous availability of nearly simultaneous satellite imagery and automated lidar measurements that triggered the present work. The goals of this study are to provide further insight into the processes responsible for such transformations and to combine them with prior literature in the hope of attaining a more robust synthesis of the mechanisms than would otherwise be possible.

2. Observations

a. Photograph

At about 1100 LT (1500 UTC) on 7 September 2003 the lead author noticed a series of contrails apparently emanating from some point to the southwest of his residence in Silver Spring, Maryland. Some of these had already been converted to cirrus uncinus with fallstreaks and others were being transformed as he watched. At about 1530 UTC he began to photograph these clouds for their aesthetic interest with no intent to study them scientifically. Thus, he did not record the exact time. Figure 1 was taken toward the south at a central elevation of about 25°. There are four lines of clouds (1–4), and probably a fifth (5), that appear to emerge from the southwest in the lower right corner of the picture. All of these had been contrails during the previous hour as he watched. Otherwise the sky was clear. The youngest of these is obviously 1.

To obtain the geometric structure of the clouds we used a telescope to measure the elevation angles of points X and Y on the building at the left. The azimuth angles were measured with a compass and corrected for the 12° magnetic declination west of true north. Using the 10-km height of the cloud-generating level obtained from the lidar (see Fig. 5) we computed the horizontal scales (L) on the right of Fig. 1 from $\tan(\psi) = (10/L)$, where ψ is the elevation angle and L is the horizontal distance from the zenith point above the observer. To estimate distances from left to right across the image use the portion of the scale centered at the appropriate elevation angle. As the elevation angle decreases one sees that the spacing of the cloud lines 1 and 2 is ≈5 km regardless of the angle of view. In short, they are parallel to one another; their apparent convergence is due only to perspective. The same is true for the other cloud lines. We shall discuss the size of the cloud elements later.

The reader may obtain the true orientation from Fig. 1 by viewing the picture as if it is overhead. The bottom of Fig. 1 is toward the south, the top is north, the left is east, and the right is west. These directions are marked on Fig. 1. For ease of interpretation simply flip the photo around its vertical axis. One sees that the cloud lines are crossing the field of view from southwest to northeast. A second cloud photo was taken a few minutes after that in Fig. 1 at a higher elevation angle with the telephoto lens (not shown). This showed a portion of the cloud image at a higher resolution, but with little new information other than the movement of the identifiable cloud features toward the northeast along the cloud lines. In future experiments it would be useful to record the changes in elevation and focal length between successive photographs to determine cloud motion.

b. Satellite observations

Figure 2 is an image taken with the visible channel of the Moderate-Resolution Imaging Spectroradiometer (MODIS) on board the *Terra* satellite at 1610–1615 UTC about 40–45 min after the photo in Fig. 1. The image was taken with band 1 at a central wavelength of 0.645 μm and a spatial resolution of 250 m. Distances are shown on the scale at the bottom. The triangles mark the locations of the Washington Dulles International Airport, Virginia, the Atlas residence, and the Goddard Space Flight Center (GSFC), the location of the lidar discussed below. The distance between the Atlas residence and the lidar is 10 km. There is a group of five quite distinct contrails extending about 18 km eastward from Dulles Airport. A sixth thin contrail, probably the youngest, is barely visible just to the west of Dulles. It runs from 38.94°N at the left boundary to 77.08°W at the top boundary. Another set of contrails starts at the Atlas residence and extends eastward for a distance of 20 km. Thus, there are two distinct areas of contrails, which we shall refer to as the west and east corridors. The contrails in the western sector are clearly

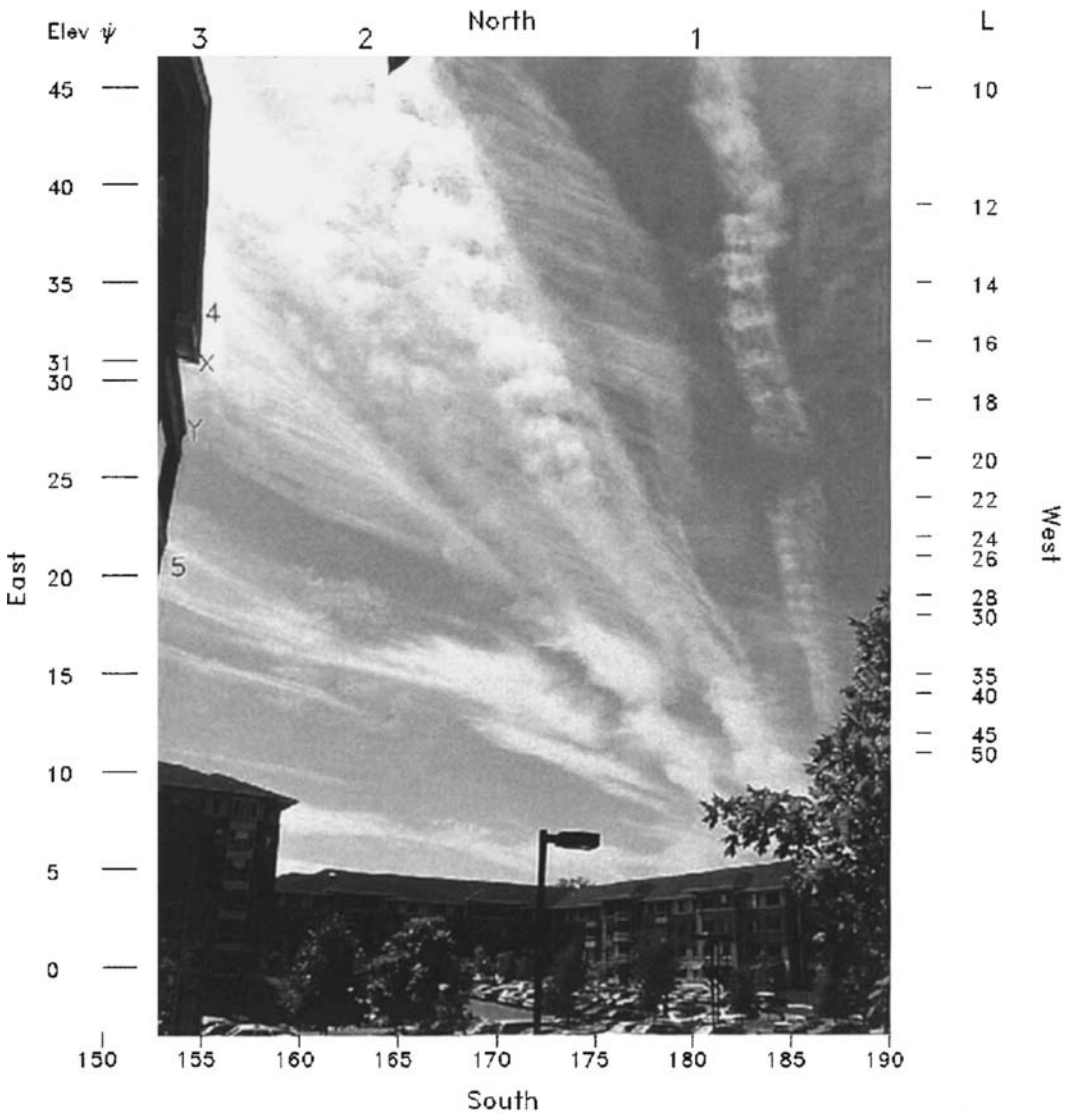

FIG. 1. Cirrus cloud streets generated from contrails. The image was taken at ≈1530 UTC 7 Sep 2003 from the Atlas residence looking toward the south. The cloud streets are labeled 1–5. Points X and Y on the building at the left represent calibration elevation angles for the scale on the left. The scale on the right represents the horizontal scale L, the distance from the zenith point over the observer at the 10.4-km height of the top of the clouds. Cloud street 1 is ≈ 20 min old and was formed in the eastern flight sector; street 2 is ≈ 2 h old and originated in the western sector (see Fig. 3).

more distinct than those in the eastern one. The latter are considerably more diffuse than those in the west and overlap each other partially.

Fortuitously, we were informed by a reviewer that Garber et al. (2005) have prepared a paper describing a flight-track database for studies of upper-tropospheric aircraft emissions over the United States and southern Canada (information is available online at http://www-angler.larc.nasa.gov/flighttracks). We have used this database to prepare Figs. 3a and 3b, which show the flight tracks in the western and eastern flight corridors, respectively. The orientation of individual flight tracks (and their contrails) ranges from 44° to 54°. Table 1 shows the aircraft corresponding to all the tracks in Fig. 3.

Those aircraft tracks in the second column of Table 1 that are marked by a "W" or "E" correspond to Delta airline flights from the New York, New Jersey, and Boston, Massachusetts, airports to Atlanta, Georgia, and several flights along the same route to more distant terminals. They are the farthest from GSFC and make up the tracks in the western corridor (Fig. 3a). The remaining flights are mostly from the same airports

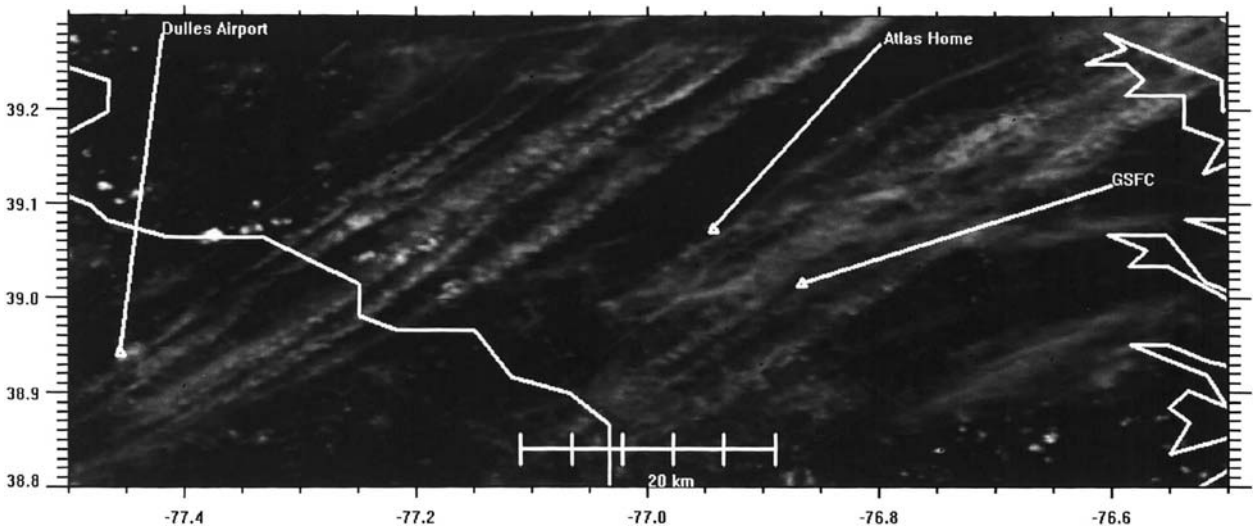

FIG. 2. The MODIS image from the *Terra* satellite at 1610–1615 UTC 7 Sep 2003. The locations of Dulles International Airport, the Atlas residence, and GSFC, the location of the lidar, are shown. Note the parallel series of contrail-generated cirrus running from southwest to northeast. (See text for details.)

with destinations in Florida, Charleston, South Carolina, and Augusta, Georgia, and occur in the eastern corridor. All flights are at a height of 10.7 km; this is very close to the tops of the contrails and associated fallstreaks shown by the GSFC lidar (see Fig. 5). Although the flights in each corridor follow one another along almost identical paths, the contrails seen in Fig. 2 are spread out from west to east. We shall see that this is because of the southeastward component of the wind, which carries them away from the original aircraft tracks.

With exception of the youngest poorly visible trail, the group of five in the western corridor cover a distance of 18 km normal to their length and are spaced about 3.6 km apart on average. The spacing is slightly less than that deduced from the photo in Fig. 1. However, most of the contrails in the satellite image occurred earlier than those seen in Fig. 1. The contrails become broader and more diffuse from west to east, consistent with their likely aging as discussed later. The second thinnest one is at the western edge of the group and passes over Dulles Airport. It is thinner at its southern end, consistent with the fact that it is the newest part of the trail behind the southerly flying aircraft. Its width is slightly greater than the 250-m pixel dimension. The youngest trail begins over 38.65°N latitude, 77.77°W longitude. This may be the position at which the aircraft reaches the altitude and/or latitude at which the aircraft trails become saturated with respect to ice and allows them to persist. The humidity will be discussed further below. Once we view the lidar records shown in the section 2c, we shall discuss the associa-

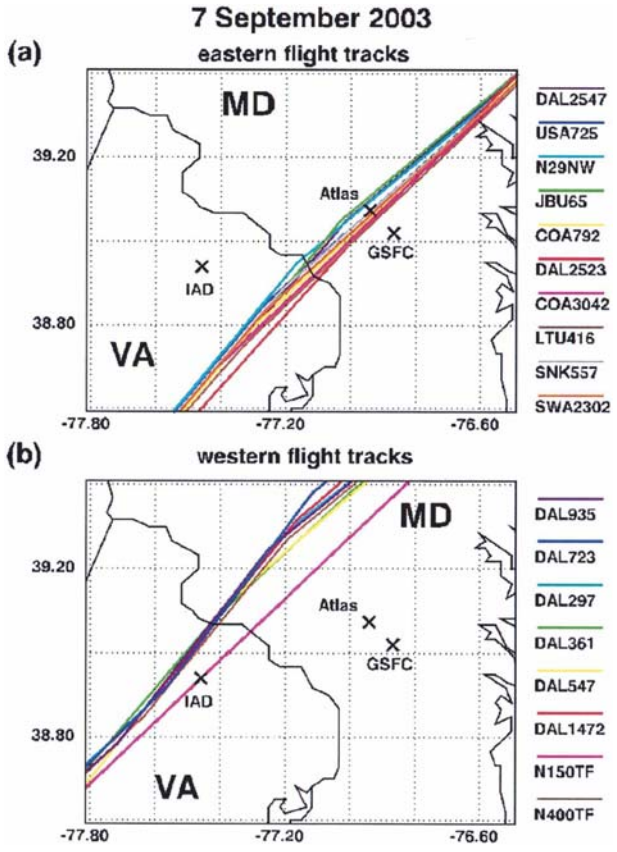

FIG. 3. Flight tracks in (a) eastern and (b) western corridors. The color code corresponds to the aircraft flight shown at the right. (See Table 1 and text for details.)

TABLE 1. Aircraft, their contrails, distances from noted points, and their arrival times at GSFC. Those contrails that occurred in the western corridor are labeled as "W"; those in the eastern corridor are labeled "E." The flight tracks run essentially northeast to southwest. The eastward distances from the track to Atlas's home and to GSFC are measured from the point in the flight track on the same latitude. The negative distances indicate that Atlas is west of the contrails at the time of the satellite overpass of 1615 UTC. The column marked ΔT is the time required for the contrail to move from the aircraft track to Goddard. See appendix for definitions of other abbreviations.

Flight number	West–east group	Flight track	Time at Atlas home (decimal UTC)	Flight height (km)	Distance to Atlas home (km)	Distance to GSFC (km)	ΔT to GSFC (h)	Time of arrival at GSFC (decimal UTC)
DAL361	W	EWR–ATL	13.557	10.67	51.56	68.66	1.94	15.50
DAL297	W	LGA–ATL	13.914	10.7	52.46	67.66	1.49	15.40
DAL723	W	BDL–ATL	14.536	10.7	52.16	66.90	1.40	15.93
DAL935	W	BOS–ATL	14.497	10.7	51.56	68.03	1.76	16.25
DAL547	W	PVD–ATL	13.244	10.67	50.69	67.81	1.93	15.17
DAL1472	W	LGA–ATL	15.021	10.67	52.53	67.73	1.49	16.51
N150TF	W	TEB–BHM	15.524	10.67	36.31	53.62	1.57	17.09
N400TF	W	TEB–4R4	15.774	10.75	47.54	63.53	1.54	17.31
LTU416	E	EDDL–CUN	16.799	10.858	−5.33	15.89	0.34	17.14
N29NW	E	HPN–AHN	15.584	10.60	−8.96	7.59	0.20	15.78
SNK557	E	EWR–IE	16.664	10.60	−12.06	4.66	0.12	16.79
SWA2302	E	BDL–TPA	17.307	10.52	−10.63	5.96	0.16	17.46
COA792	E	EWR–MCO	15.008	10.67	−3.07	14.31	0.42	15.43
COA3042	E	EWR–TPA	14.380	10.67	−4.48	11.88	0.37	14.76
DAL2523	E	BOS–TPA	14.949	10.67	−6.19	10.26	0.26	15.21
DAL2547	E	LGA–TPA	16.297	10.67	−1.69	14.87	0.39	16.69
JBU65	E	JFK–TPA	15.281	10.7	−3.91	12.94	0.35	15.63
USA725	E	BOS–CLT	15.919	10.7	−6.14	11.19	0.33	16.25

tion of the aircraft contrails with those detected by the lidar.

Meanwhile one may see the rather fairly regularly spaced bright spots in the contrails in the western corridor. These are the generator tufts of the cirrus uncinus that are also seen clearly in cloud line 2 of Fig. 1. Their spacing is ≈1.4 km, close to the 1.5-km spacing in Fig. 1. Careful viewing shows that there is a less bright veil of clouds to the west or northwest of the contrails. These correspond to the fallstreaks that are seen to the northwest of the contrail 2 in Fig. 1.

c. Radiosonde data

Figure 4 presents the radiosonde soundings at Sterling, Virginia (adjacent to Dulles Airport in Fig. 2), at 1200 UTC 7 September (solid) and 0000 UTC 8 September 2003 (dashed). The photo in Fig. 1 was taken about 4.5 h after the first sounding and 7.5 h before the second, respectively. The profiles of temperature, wind speed, and direction are very similar at both times. Only the relative humidity increased significantly during the day. The dotted profile of RH represents the saturation relative humidity with respect to ice (RH_i) in both soundings. The environment is supersaturated with respect to ice between 7.2 and 10 km at 0000 UTC and is very dry below 7.2 km. From the lidar observations to be discussed below (Figs. 5 and 6) the contrails occurred near 10-km altitude. Because persistent contrails require RH_i 100%, the humidity must have reached this value some time in the morning hours prior to the visual observations. The exact RH_i at the time of formation is not known. Based upon the 0000 UTC, the mean RH_i between 7.3 and 9.8 km is 108%. However, it is well known that radiosondes underestimate upper-tropospheric humidity by as much as 60% at typical contrail formation temperatures from −40° to −50°C (Miloshevich et al. 2001). Furthermore, we shall see that the humidity is enhanced by the vertical motions that generate the cloud (Jensen et al. 1998).

d. Lidar

When the contrails moved over GSFC, the micropulse lidar (MPL) captured the vertical structure of the generators and their fallstreaks. Table 2 presents the characteristics of the lidar. Figure 5 shows the time–height indicator (THI) display of the attenuated lidar scattering ratio (ALSR) of the clouds. ALSR is the ratio of MPL total attenuated backscattering signal to the molecular backscattering signal (MBS). The MBS is approximated by the signal from the clear-sky period just before the contrails moved in. The temporal resolution of the lidar data is 1 min. The record covers the period between 1330 and 1836 UTC. Another record of the lidar observations is shown in Fig. 6, which deals

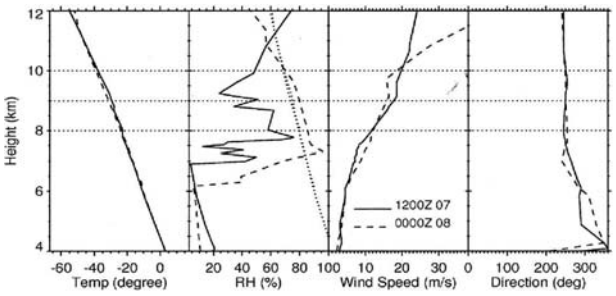

FIG. 4. Radiosonde soundings taken at Sterling, VA (adjacent to Dulles Airport) at 1200 UTC 7 Sep 2003 (solid) and 0000 UTC 8 Sep (dashed). The dotted curve is the saturation relative humidity with respect to ice. From left to right the panels represent temperature, relative humidity, wind speed, and direction. (See text for details.)

with the detailed microphysical and radiation properties of the fallstreaks A–G in Fig. 5. The latter figure will be discussed in detail in section 3c.

We first determine the probable generating level and the base of the cirrus trails. The vertical turret at the top of each precipitation trail corresponds to a convective-generating cell. Each such element extends from 10.0 to 10.4 km, except for the first two that extend about 200 m higher. Such convective clouds move with the winds near their base (Gunn and Marshall 1955; Douglas et al. 1957). Thus, the 10-km height is the effective generating level. From Fig. 2 one sees that the contrail is oriented from 232° to 52°. The 1200 UTC wind is 20 m s^{-1} from 250° so that the speed along the trail is 20 cos18 = 19.0 m s^{-1}. The speed normal to its length is 20 sin18 = 6.2 m s^{-1}. We remind the reader that the aircraft are flying *toward* the southwest while the winds are coming from that direction.

Note that the bases of the fallstreaks lower with time between 1400 and 1700 UTC, after which the bases remain constant. Of course, the bottoms represent the height of evaporation of the ice crystals, thus suggesting that the relative humidity is increasing during the afternoon at the lower levels. Because all of the other parameters in the soundings of Fig. 4 remain the same for 12 h after 1200 UTC, it is likely that the evaporation of the fallstreaks is causing the downward increase of RH. This has been noted previously by Minnis (2003).

The fallstreaks shown by the lidar are ≈12 min apart. With a wind speed component of 6.2 m s^{-1} normal to the contrails, the spacing corresponds to a distance of 4.5 km very close to that found in Figs. 1 and 2. In other words, each fallstreak seen by the lidar is essentially a vertical cross section at somewhat less than 90° to the contrail.

Allowing for the 1-min resolution, the turrets of each fallstreak are 3–5 pixels wide in time. Each pixel corresponds to 1 min so that the width of the turret ranges between 180 and 300 s. With the 6.2 m s^{-1} crosswind the turrets are 1–2 km wide. These correspond to the convective elements in Figs. 1 and 2 observed earlier and with the speckled generator elements that can be seen in the thinner contrails of Fig. 2. The heights of the turrets are 400–600 m. The numerical simulation of Jensen et al. (1998) shows that the turrets of the cirrus uncinus grow vertically to a depth of 500 m after 60 min. However, the rate of growth is dependent upon RH_i.

In the THI record of Fig. 5 one sees that the vertical dimension of the fallstreaks is typically 2 km. Using a minimum fall speed of 0.5 m s^{-1} (normalized to surface pressure) as found below from the slope of the streaks, the lifetime of the generators must be at least ≈4000 s.

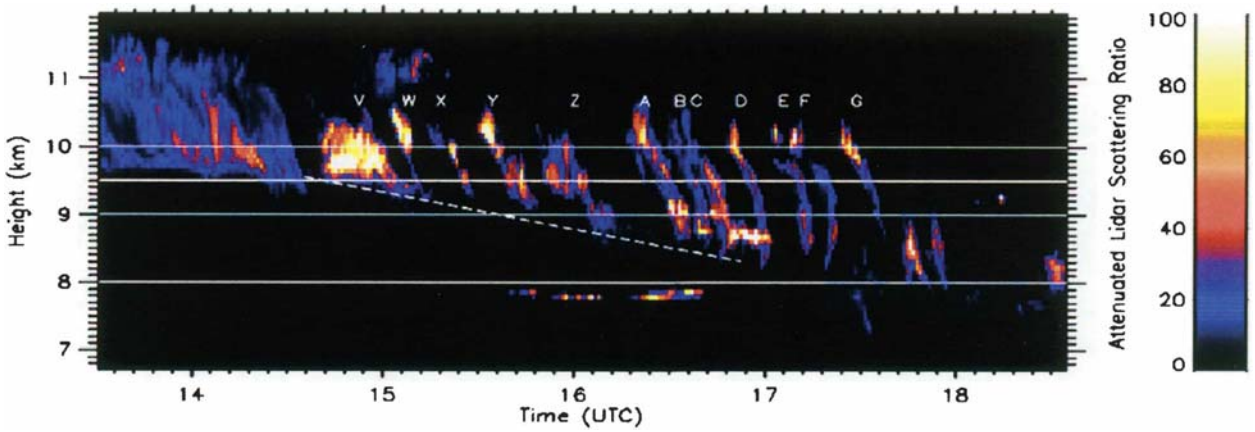

FIG. 5. Observations taken with the MPL lidar at GSFC between 1330 and 1836 UTC (shown in decimal hours). Fallstreaks A–G correspond to those shown in Fig. 6. Fallstreaks V, W, X, and Z are included here for later determination of their relation to contrails produced by the aircraft. Horizontal line at 10 km corresponds to base of the generator turrets of the cirrus uncinus. That at 8 km corresponds to the bottom of the fallstreaks after 1700 UTC. The dashed line shows the descent of the bottom of the fallstreaks with time as moisture is transferred downward from above.

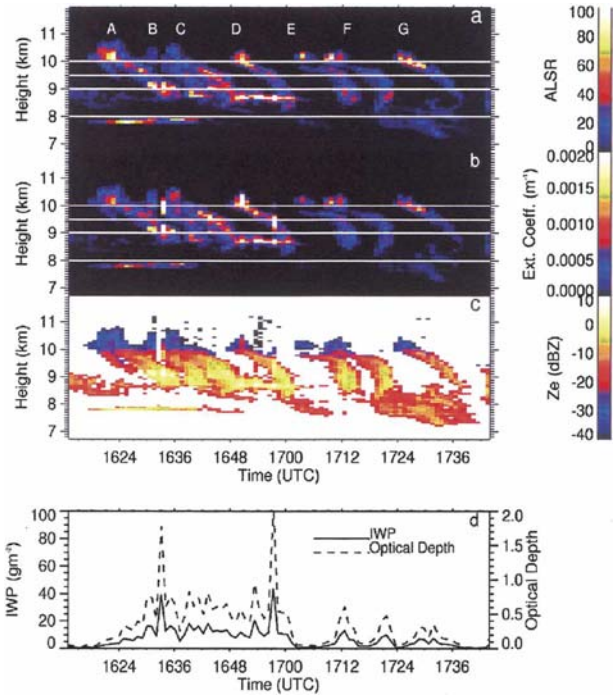

FIG. 6. The lidar observations taken at GSFC between 1612 and 1745 UTC for calculations of microphysical and radiative properties: (a) basic data, ALSR for fallstreaks A–G; (b) the extinction coefficient; (c) the estimated radar reflectivity factor computed from the data in (b); and (d) the corresponding IWP (left scale and solid curve) and optical depth (τ) (right scale and dashed curve).

It will be shown later that they persist considerably longer.

3. Interpretation

a. Contrail orientation and spacing

From the Figs. 1, 2, and 3a we have seen that the contrails are oriented toward the northeast. Their spacing is ≈4–5 km. The motion of the base of the fallstreaks is toward ≈58°, consistent with the winds at and below the generating level, and the orientation of the bands.

The horizontal dimension of the tufts in line 1 is ≈1 km and their spacing is also ≈1 km regardless of ψ. The older contrail clouds in line 2 have dimensions of ≈1 by 2 km at all ψ. And the largest dimension of the ice crystal fallstreaks are typically 2 km wide. Similarly, we have seen that all of the prior cloud lines (1, 2, 3) are parallel to one another although their spacing depends upon their relative age, that is, the time between successive aircraft flights.

As noted above the tufts in young line 1 are reminiscent of those often seen in young contrails. These have been shown to be the result of the aircraft wake dynamics and the subsequent Brunt–Väisälä oscillations of the older wake plumes (Lewellen and Lewellen 2001). In their simulation they found that the pendants of young contrails are spaced about 300 m apart. The pendants are composed of a large concentration of tiny ice crystals and large ice water contents. It is these that are heated by longwave radiation from the ground and grow to become the generator elements of the cirrus uncinus.

TABLE 2. MPL lidar parameters.

Parameter	Value
Wavelength	0.523 μm
Pulse length	≈10 ns (3 m)
Output energy	10 μJ
Pulse repetition frequency	2500 Hz
Transceiver aperture	0.2 m
Field of view	100 μrad
Filter width	0.27 nm
Range resolution	30 m
Averaging time	60 s

The veil of cirrus to the northwest of line 2 is striated by fairly regularly spaced bright fallstreaks against a background of rather uniform and diffuse field of lesser brightness. The number of bright streaks that appear to be emanating from line 2 is very nearly twice the number of cumuliform turrets in that line. There are two possible explanations for this behavior. First, recalling that the bottom of the fallstreaks are near 8 km at the time of Fig. 1 they must have started their fall some 67–35 min earlier, assuming fall speeds between 0.5 and 1.3 m s^{-1}, respectively. Thus, the generators from which they fell were considerably younger and probably appeared similar in nature to those in line 1 when they started to release the ice crystals. There are 12 or 13 bright striations in the fallstreaks associated with line 2. This corresponds reasonably well to the number of tufts in line 1 in the same distance at the 10.4-km level. (We must be cautious in making such a comparison because each line was probably generated by another aircraft with different wake structure and thus tuft spacing.)

It is clear that the more mature cumuliform elements in line 2 are much larger than those in line 1 (Jensen et al. 1998). This is consistent with the fact that the cloud elements are growing. Knollenberg (1972) attributed such growth to the release of latent heat. However, for ice water contents of 0.1 g m^{-3}, such as reported below, the latent heating is only about 0.13°C. Jensen et al. (1998) suggest that the heating is due mainly to upwelling longwave radiation from the warm surface and that latent heating is negligible.

In the Jensen et al. (1998) model the generating tur-

rets grow at a maximum vertical velocity of 5–8 cm s^{-1}, thus accounting for the growth of a few hundred meters in the first hour. In addition, they show that the updraft extends through a larger vertical extent than the heating itself. Hence, just above the contrail core, the vertical motion drives adiabatic cooling and an increase in humidity. Relative humidity with respect to ice as large as 150% was generated within 1 h. In view of the rather low RH_i of 108% computed from the soundings, the rapid growth of the cirrus clouds observed in the present case is likely to be the result of the latter mechanism.

Returning to the question of the fairly regularly spaced and numerous bright striations of the fallstreaks, another alternative explanation is suggested by the work of Heymsfield et al. (1998). They propose that the high concentrations of small crystals within the core of the contrail reduces the vapor density to saturation, leaving localized regions of supersaturation along the contrail periphery where crystals grow rapidly to several hundred microns and precipitate out in the form of fallstreaks. This process could lead to the production of two fallstreaks for each generating cell, possibly accounting for the approximate 2:1 ratio of cloud turrets to fallstreaks.

Jensen et al. (1998) also cite a similar process for the sorting of the crystal sizes with fall speed and shear. Their plate 3 shows maximum ice water content (IWC) at the upper edge of the fallstreak. This is where we also find the maximum backscatter and extinction coefficient in fallstreaks C and D in the lidar Figs. 5 and 6.

When viewed from the side (not shown) the clouds had the form of regularly spaced cirrus uncinus. At first viewing, it was thought that the bright cumuliform elements must be composed of water. But this is unlikely at −40°C, the temperature at which homogenous nucleation occurs, so that water drops formed in the contrail must freeze within a few seconds (Heymsfield and Sabin 1989; Schröder et al. 2000). Like Heymsfield et al. (1998), in situ observations of contrails in transition to cirrus by Schröder et al. (2000) have shown that contrails are dominated by high concentrations (>100 cm^{-3}) of nearly spherical ice crystals with mean diameters in the range of 1–10 μm. This implies that the cumuliform turrets have very large extinction coefficients and are almost as bright as those of warm cumulus. The observations of Heymsfield et al. (1998) are similar to the results of the simulations by Gierens (1996).

To put the above discussion into context Fig. 7 presents a three-dimensional schematic of contrail 2 and its fallstreaks, along with the associated winds. In order that the pattern be consistent with the photo of Fig. 1

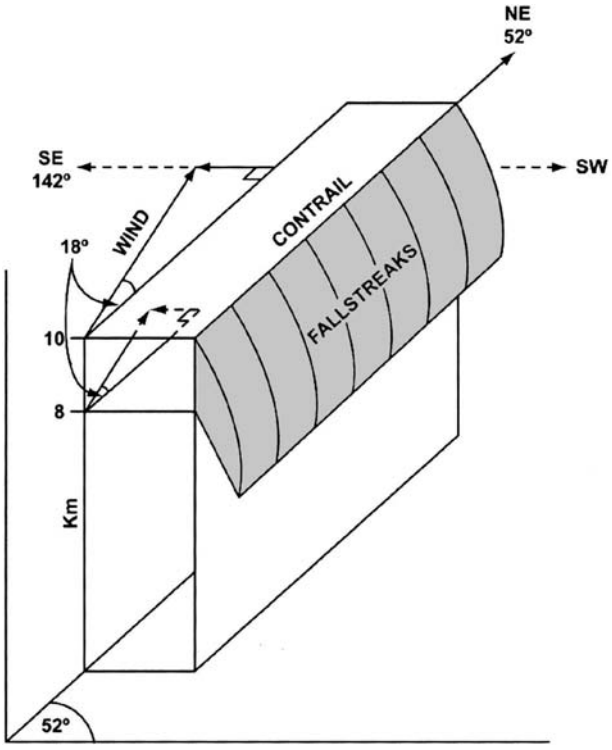

FIG. 7. Schematic diagram contrail cirrus and associated fallstreaks oriented in a manner corresponding to the image of contrail B in Fig. 1. The contrail is aligned along 52° as observed in Fig. 2 and the azimuth angle increases *counterclockwise*. The winds at the 8- and 10-km levels and their crosswind components are shown. (See text for details.)

we have set the horizontal axis pointing toward 0° (actually toward the southwest). Because southeast is toward the left in Fig. 1 and the contrail is oriented toward the northeast, the angle increases counterclockwise as it does in the photograph. The wind vectors are indicated by the arrows and are plotted in the horizontal planes at their corresponding heights. The wind directions at both the 8- and 10-km levels are almost identical from 250° (i.e., toward 70°); the speed is 20 m s^{-1} at 10 km and 12 m s^{-1} at 8 km.

At the 10-km level the wind component normal to the contrail is 20 sin18 = 6.2 m s^{-1} and is directed at (52 + 90) = 142°. Thus, each element of the contrail moves to the northeast (i.e., toward the left in Fig. 7) as also shown in the visual photograph of Fig. 1 and the satellite image in Fig. 2. However, the entire contrail is advected toward the southeast with a component of 6.2 m s^{-1}, or to the east with a component of ≈10 m s^{-1}. At heights below 10 km, the component of the wind normal to the contrail is smaller so the fallstreaks trail behind the contrail (i.e., toward the southwest). In addition, the wind along the contrail is less than it is at the generating level, so the fallstreak also trails off be-

hind the generator along a line parallel to the 52° direction. The combination accounts for the curvature of the fallstreaks.

b. *Correlation of aircraft tracks and observed contrails*

We now return to the correlation of the aircraft tracks and their contrails to the fallstreaks emanating from the contrail cirrus as observed by the lidar. The steps are straightforward. 1) Plot the aircraft tracks as shown in Figs. 3a and 3b and listed in Table 1. 2) Find the position and time of the track directly west of GSFC, as listed in Table 1; this can be converted to the perpendicular distance between contrail and GSFC by using the contrail (i.e., the flight) orientation. 3) Compute the time of travel of the track (and its contrail) eastward to reach the lidar at GSFC by using the perpendicular distance in step 2 and corresponding wind speed. The orientation of each contrail is calculated based on the flight track as indicated in Fig. 3. 4) Add the time of travel from step 3 to that found in step 2 to get the predicted time of arrival of the contrail over the lidar, also shown in Table 1. This approach assumes a constant wind velocity between the aircraft tracks and GSFC; however, the results show that this assumption is reasonable.

Figure 8 shows the scatterplot of the estimated versus actual contrail arrival times at the MPL at GSFC. The large dots correspond to contrails produced by different aircraft. Alongside of each dot is the flight number as given in Table 1. Those that started in the western corridor (Fig. 3a) are indicated by flight numbers shown to the left of each circle, and conversely. The corresponding contrails are shown by the alphabetical letters A–G and V–Z as seen in Fig. 5. One sees an excellent time correlation of the predicted and observed contrails with few exceptions. The correlation coefficient is 0.99. Note that the 18-min duration contrail between 15.60 and 15.90 UTC includes four predicted aircraft trails—DAL2229 and N29W from the western corridor, and JBU65 and JBU129 from the eastern sector. This indicates the nearly simultaneous arrival of contrails that started earlier at greater distances upwind with those that started later at lesser distances from GSFC. This broad contrail is identified as Z in the lidar record of Fig. 5. It shows two adjacent highlights in its fallstreak, a good sign of the joining of two or more contrails. Also note that any of the contrails estimated to arrive after the satellite pass (1615 UTC or 16.25 in decimal hours) will not be seen in the satellite image of Fig. 2.

Now compare the distances from the Atlas home in Table 1 (column 6) with the contrail positions on the satellite image in the 1625 UTC overpass. By plotting the distances of the flight paths from Atlas (column 6) on an overlay, one finds that that there are no corresponding visible contrails in Fig. 2 more than 33 km westward of the Atlas home. Instead, the first of the six flights in Table 1 appears to match the western boundary of the visible contrails. The difference between the most distant flight to the west (DAL1472) at 52.53 km and the most distant visible contrail at 33 km west, is 20 km. The time of eastward travel from the aircraft position to that of initial detection of the contrail by MODIS is thus $\approx$(20 km/0.01 km s^{-1}) $\approx$33 min. This is a reasonable time for growth to detectability.

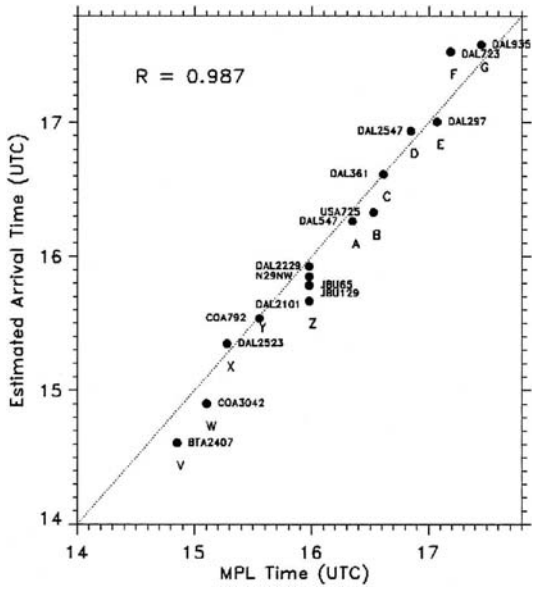

FIG. 8. The scatterplot of estimated vs actual contrail arrival times at the MPL lidar at GSFC. Large dots represent the contrails produced by the aircraft flights marked adjacent to them. Flight identifiers to the left of the dots started in the western flight corridor; those to the right of the dots originated in the eastern flight corridor. The correlation coefficient is 0.99.

In short, the total coverage of the contrails is truncated on the eastern end by the distance of travel for growth to detectability and on the western end by the time of the satellite overpass, or the end of the lifetime of the contrail, whichever occurs earlier. The total east–west line of contrails is thus limited to 55 rather than 65 km. Except for the broad contrail found between 1 and 6 km west of GSFC in Fig. 2, which we have associated with the four contrails between 15.60 and 15.90 UTC in Fig. 8, we have not been able to make a one-to-one correlation with those on the satellite image. The best that can be done is to indicate that there are five distinctly detectable contrails on the satellite, and four aircraft flights in the 1-h interval, corresponding to total of 26 km and an average east–west spacing of 6.5 km, or

4.0 km normal to the contrail orientation as mentioned earlier.

The age of the contrails is indicated by those originating in the western corridor at distances of 61–69 km west of GSFC. These required travel times up to 2 h after generation and demonstrate the minimum contrail lifetime because they must have survived after passing GSFC.

Persistence of contrails has been reported by many authors as follows: (a) >1 h, Knollenberg (1972); (b) >2 h, Konrad and Howard (1974); (c) 6 h, Heymsfield et al. (1998); and (d) 17 h, Minnis et al. (1998). Boin and Levkov (1994) have found a nearly exponential increase of the lifetime with increasing humidity. The optical thickness also increases sharply with RH_i (Jensen et al. 1998).

c. Microphysical and optical properties

We now move on to the lidar observations in Fig. 6. As noted earlier, the fallstreak generators are just above 10-km level with ALSR >50 most of the time. In the fallstreaks ALSR ≈20. Note that the initial generator and fallstreak A occurs between 1618 and 1636 UTC, about 40–60 min after the cloud photographs. Using the 6.2 m s^{-1} component of the wind speed of the contrail, each trail that passes over the Atlas residence reaches the lidar ≈27 min later. Thus, the lidar observes the same fallstreaks as those that were seen earlier by Atlas (Fig. 1) although at later times in their life cycle. Note that the 6.2 m s^{-1} wind speed component assumes the predominant flight orientation of 52°; the latter orientation will be used in further discussion unless indicated otherwise.

The ALSR can be converted simply to the extinction coefficient by using an extinction-to-backscattering ratio (lidar ratio) and molecular backscattering coefficient estimated from the radiosonde profiles. The lidar ratio for cirrus clouds varies and is slightly dependent on temperature (Whiteman et al. 2004). However, the mean value for ice clouds is ~18. As an approximation, we use this value to convert ALSR to the extinction coefficient. Because of the weak MPL signal during daytime, forward integration was used for attenuation correction. This procedure works well for optical depth below 0.8 in this study; it is not stable for larger values (Klett 1981). Fortunately, there are only three unstable cases during this period. The estimated extinction coefficients are shown in Fig. 6b. The results of the simple forward integration were compared with the Klett backward solution for profiles with clear air above cloud top. The two approaches agreed well. Although the uncertainty of any data point may be as large as ±50% because of the natural variation of the cirrus lidar ratio, the mean extinction coefficient and vertically integrated optical thickness are more accurate.

To determine the IWC profiles one may use Eq. (16) from Atlas et al. (1995). This is

$$\sigma = (3.5/\rho_i)(\mathrm{IWC}/D_0). \tag{1}$$

Here, they assumed a gamma function size distribution with a dispersion factor $\mu = 1$, a ratio of the median volume to effective particle diameters of 1.17, and an extinction efficiency for all particles $E = 2$. For particle density, they also used $\rho_i = 140\,(D_0)^{-1}$ from Brown and Francis (1995). The latter relation actually applies to individual particles; it is only applicable to D_0 for narrow distributions. In the present case therefore it is an approximation; the same is true for Eq. (1). Because the temporal resolution of the lidar is 60 s, or about 360 m at the speed of the crosswind component, and the vertical resolution is 100 m, the lidar observations encompass a vast number of particles so that the individual measurements correspond to a volumetric average that is not likely to be much different than D_0. Thus, from (1) we may estimate the IWC using values of σ and D_0.

The fall speeds were obtained from the slope of the fallstreaks on the THI lidar records using the following relation:

$$V(h) = \frac{[W(h) - W_g]}{(W_g)} \frac{\Delta h}{\Delta t}, \tag{2}$$

where $V(h)$ is the fall speed, W_g is the wind speed at the generator level, $W(h)$ is the wind speed at height h, and $\Delta h/\Delta t$ is the slope of the fallstreak at height h on the THI. The winds were taken from the 0000 UTC sounding. We used the upper and lower boundaries of the fallstreaks as in Fig. 9a because these boundaries represent the smaller and larger particles, respectively. The fall speeds are normalized to surface pressure. Figure 9b presents the fall speed as a function of cloud height and indicates that speed increases downward. The values range from 0.4 to 1.4 m s^{-1} and are similar to those reported by Konrad and Howard (1974).

The particle median volume diameters D_0 were estimated from the relationships of Matrosov et al. (2002). Figure 9c shows that D_0 ranges from ≈70 to 1200 μm. The latter are comparable to in situ measurements of Heymsfield et al. (1998) and Knollenberg (1972), although both report actual particle sizes and not D_0. Last, Fig. 9d presents a scattergram of the coefficient $K = (\sigma/\mathrm{IWC})$, the relative importance of the extinction coefficient as compared with the ice water content, versus height for fallstreak C.

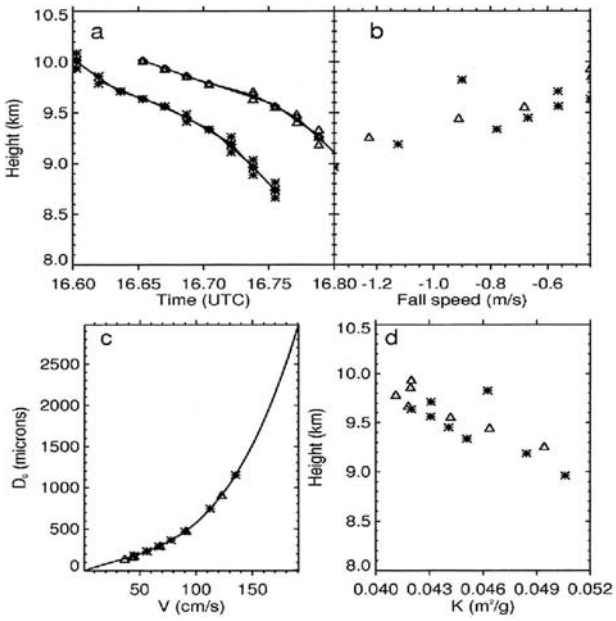

FIG. 9. (a) Time–height profiles of the top (triangles) and bottom (asterisks) of fallstreak C determined from Fig. 5a; (b) the particle fall speed, normalized to surface pressure, computed from (a); (c) the median volume particle diameter computed from the fall speed in (b); and (d) the coefficient K, the ratio of the extinction coefficient to ice water content as a function of height.

The latter approach has been conducted for all seven fallstreaks in Fig. 6. The results show that $0.04 < K < 0.05$ m^2 g^{-1}, as in Fig. 9d, with the exception of a few outliers. The values of K reported by Heymsfield et al. (2003) for midlatitude cirrus fall in the same range. Moreover, the smallest values of the extinction coefficient (σ), IWC, and Z reported by the latter authors are $\approx$0.0004 m^{-1}, 0.003 g m^{-3}, and -20 dBZ, respectively. These correspond closely to the same parameters in the present study. In other words, the microphysical properties of the contrails are similar to those of the more tenuous midlatitude cirrus. With some exceptions this is the qualitative impression one gets when viewing the sun through contrail-generated fallstreaks. They only rarely have optical thickness as large as 1 (Minnis 2003).

Figure 6b presents the profiles of optical extinction coefficient σ, which range from 0.0005 to 0.002 m^{-1} during the 93-min period. The largest values typically occur in the generator heads where the particle concentrations are very large and sizes are small (Heymsfield et al. 1998; Schröder et al. 2000). Figure 6d shows the optical thickness (τ, dashed) and the IWP (solid) as a function of time; τ is the vertical integral of σ over height while the IWP is the corresponding integral of IWC obtained from Eq. (1). Clearly, the peaks of both parameters correspond to the generator heads. Table 3 presents a summary of the mean and maximum optical depths and IWP partitioned according to height. The local maximum values of τ for each of the fallstreaks range between 0.8 and 2 while the *average* of the local maxima for the seven streaks is 1.4. The average τ for the entire period is 0.35. When partitioned with respect to echo height the average optical thicknesses are 0.3 and 0.13 below and above 10 km, respectively. Clearly, the fallstreaks, which occur below 10 km, contribute most to the average optical thickness.

For comparison, the optical thickness for contrails and associated falltreaks reported by various authors are (a) $\approx$0.1, Knollenberg (1972); (b) 0.2–0.8, Minnis et al. (1998); (c) maximum $\approx$0.5 and average $\approx$0.2, Khvorostyanov and Sassen (1998); and (d) 0.1–0.6, Duda et al. (2004). The agreement is quite reasonable. However, one may expect greater variability because of changes in IWP with ambient conditions and age of the contrails. The simulations of Jensen et al. (1998) with a variety of initial conditions result in average values of τ ranging from 0.01 to 0.053 and maximum values ranging from 0.15 to 0.46. The largest values correspond to the largest assumed initial values of RH$_i$. The present values of τ, and those of prior observers, are closer to the maxima of Jensen et al. (1998) rather than to their average values. From Table 3, the ratio of IWP/τ = 23.1 versus 21.0 from Heymsfield et al. (2003, their Fig. 7a) at the lower portion of the range of midlatitude cirrus clouds.

Now consider the IWP. From Table 3 the average IWP is 8.14 g m^{-2}. This is distributed over the 2-km length of the fallstreaks. Accordingly, the ice water per meter (IW m^{-1}) of flight is 1.63×10^4 g m^{-1}. This compares to the amounts of water released by various aircraft as estimated by a number of authors: (a) 1.73 g m^{-1}, Sabreliner (Knollenberg 1972); and (b) 13.3–14 g m^{-1}, B747 (Gierens 1996; Gierens and Jensen 1998). In a model by Lewellen and Lewellen (2001) they find that IW m^{-1} increases rapidly after the first 100 s to values of 1–3 g m^{-1} at 2000 s and an RH$_i$ = 130% for a B737 and B747, respectively, Of course, the latter values decrease at smaller ambient humidity. In any case, it is clear that the IW m^{-1} in the present case is 10^3–10^4

TABLE 3. Optical depth and ice water path.

Height (km)	Mean optical depth		Mean ice water path (g m^{-2})	
	Max	Avg	Max	Avg
All	1.4	0.352	38.6	8.14
<10		0.295		6.18
>10		0.129		2.88

times that released by the aircraft. This is no surprise when one simply compares the size of the cirrus uncinus with that of the initial contrail.

d. Radar reflectivity

Use of D_0 and IWC as discussed above permits the calculation of the approximate equivalent radar reflectivity factor Z_e from Eq. (10) in Atlas et al. (1995). The results are displayed in Fig. 6c. The reflectivities (in $10\text{Log}Z_e$ − dBZ, but commonly referred to only as Z_e) in the fallstreaks range from ≈−20 to +10 dBZ. However, the values in the generator turrets fall between −25 and −30 dBZ. Konrad and Howard (1974) measured the reflectivities of fallstreaks with a powerful 10.7-cm radar at Wallops Island, Virginia. They reported Z_e ranging from −14 to +16.5 dBZ, assuming beam filling; the true values would be greater if the beams were actually filled. However, it is doubtful that they could measure reflectivity as small as those deduced from the present lidar measurements.

It is of interest to compare the reported values of Z_e with the minimum detectable reflectivity for the planned CloudSat radar, that is, −26 dBZ (Stephens et al. 2002). Thus, assuming that the present estimates of Z_e are correct, the CloudSat radar will probably fail to detect the generator heads. On the other hand, the lidar planned for the Cloud–Aerosol Lidar Infrared Pathfinder Satellite Observation (CALIPSO) satellite should be able to detect both the heads and fallstreaks (Winker et al. 2003).

4. Remarks—Climatic impact

It is interesting that the mean optical depth found in this case (0.35) corresponds to that found in climatological satellite measurements by Ponater et al. (2002) and Minnis et al. (2004), and that the microphysical properties are consistent with a wide range of observations and models by prior authors. Accordingly, it is appropriate to speculate on their effect on climate.

The issue of the impact of contrail-generated cirrus (CS) on climate change has been treated by a number of investigators. Sassen (1997) suggested that the unusually small particles typical of many persistent contrails might favor the albedo cooling over the greenhouse warming. Using a 2D mesoscale cloud model Khvorostyanov and Sassen (1998) computed the distribution of the mean crystal radius, concentration, and ice water content of a contrail after 30 min of development. They found a twofold effect. At the surface, the net greenhouse minus albedo effect was negative with a cooling of 15 W m^{-2}. However, at the top of the atmosphere (corresponding to the entire atmospheric column), the net effect was a warming of 8 W m^{-2}. We note that the latter simulation for the early stage of the cloud produced very large concentrations of small crystals and that the longwave warming would be increased relative to the shortwave cooling with the much larger particles, such as found in the present study.

An evaluation of the effects of contrail cirrus over the globe is complex because of the great geographic and diurnal variability of air traffic, the variability of optical thickness and persistence of the clouds, the background brightness, and the natural changes in ambient humidity (Minnis 2003). There are also a number of feedback mechanisms at play that climate models have not dealt with very well. The finding that the vertical motions accompanying the transformation to cirrus also increase the humidity above the contrail is one such factor (Jensen et al. 1998). Nevertheless, using results from a general circulation model simulation of contrails, Minnis et al. (2004) found that the cirrus trends resulting from contrails in the United States are estimated to cause a tropospheric warming of 0.2°–0.3°C decade^{-1}, a range that includes the observed trend of 0.27°C decade^{-1} between 1975 and 1994. One must emphasize that, even if correct, this is a regional effect. We may summarize the various studies as follows:

1) regional effects in the 1990s in the United States and Europe have a cover of 0.5%–2% with a maximum over Europe of 0.35%, and warming of 0.1–0.2 W m^{-2}, and
2) global effects that are about 0.1 of the regional values.

These estimates are based upon the work of Minnis et al. (1998), Ponater et al. (2002), Palikonda et al. (2002), and Minnis et al. (2004). The latter authors also project an aircraft scenario for 2050 that would produce a regional radiative forcing of 1.5 W m^{-2} over Europe, a global coverage of 0.5%, and a radiative forcing of 0.05 W m^{-2}. In short, the present-day effects are significant regionally but in the noise globally. Further research is necessary to assess factors such as the amount of cirrus that is initiated by the contrails but not distinguishable from natural cirrus.

5. Summary and conclusions

This study of the transformation of contrails to cirrus uncinus (mares' tails) was made possible by a fortuitous and unique combination of observations by a ground-based camera, a vertically pointing lidar, satellite imagery, and a new database of aircraft flight tracks. The

photograph documented the metamorphosis of the contrails to cirrus and the formation of fallstreaks almost continuously along the contrails in directions consistent with the winds. A novel method was developed to use the visible photograph with the lidar-measured cloud heights to obtain the true orientation of the contrails and fallstreaks, their spacing, and their dimensions. Although the cirrus lines appeared to converge in the southwest, they were actually almost parallel to one another, oriented from about 232° to 52° and spaced about 4–5 km apart, as confirmed by the satellite image and by the time spacing of their passage over the lidar. The flight tracks occurred in two corridors: the western corridor corresponded to flights from east coast cities to Atlanta and others in the general vicinity; the eastern corridor flights originated mostly from the same cities to destinations in Florida and the vicinity. Although the flight tracks in each corridor followed nearly identical paths in sequence, their contrails separated in time and were advected to the southeast with the component of the wind normal to the trail.

When the contrails passed over the lidar at GSFC each appeared as a cirrus uncinus cloud with a generator turret and fallstreak of ice crystals oriented nearly normal to the length of the contrail. Using the appropriate component of the wind to extrapolate backward in time, we were able to correlate each contrail at the lidar with a specific aircraft flight with a remarkable correlation coefficient of 0.99. The older contrails from a few of the flights in the western corridor arrived at the lidar nearly simultaneously with the younger ones from the eastern corridor, thus producing broader contrail cirrus at the lidar. This is also manifested by the overlap of contrails in the eastern corridor as seen by the satellite. The lag between the initial formation and the time of first detection by MODIS is ≈33 min. The 2 h required for the contrails from the western corridor to reach the lidar at GSFC is a measure of their minimum lifetime because they persisted beyond GSFC. The lead author watched them for about 1–2 h later in the afternoon.

Among other notable features of the contrails, which have formed at about −40°C, are the convective turrets or generator cells of the cirrus uncinus that grow to 1–2-km horizontal size from the initial downward pendants created by the wake dynamics of the aircraft, as shown by other investigators. The pendants are composed of a large concentration of tiny ice crystals and large ice water content (IWC) and grow via heating by longwave radiation from the ground. The brightness of the generator cells, comparable to that of warm cumulus, is also a result of the large concentration of tiny ice particles, as deduced from the lidar observations and by in situ sampling by prior authors.

The lidar observations provided three time–height profiles: 1) the attenuated lidar scattering ratio (ALSR), 2) the extinction coefficient (σ), and 3) the radar reflectivity factor (Z). The slope of the fallstreaks provided particle fall speeds and an approximation to the particle median volume diameters (D_0). The values of σ and D_0 lead to the IWC and to the parameter $K = (\sigma/\text{IWC})$, the ratio of extinction to IWC. All of the values deduced are in reasonable agreement with those by other investigators. The vertical integrals of σ and IWC provide the optical thickness τ and ice water path (IWP), respectively. The time-averaged values (over the 93-min period observed by the lidar) are $\langle\tau\rangle = 0.352$ and $\langle\text{IWP}\rangle = 8.14$ g m^{-2} and are dominated by the fallstreaks.

The average ice water per meter along the length of the contrail is 1.6×10^4 g m^{-1}, some three to four orders of magnitude greater than the water vapor released by typical jet aircraft, also similar to previously reported values. The net effect of the water and particles released by the aircraft results in a major inadvertent modification of the atmosphere under appropriate ambient conditions. Furthermore, the evaporation of the fallstreaks at lower levels indicates the downward transfer of moisture from the upper levels where the crystals have grown.

Although most investigators favor the finding that contrail cirrus produce atmospheric warming on regional scales in the United States and Europe, the impact on global warming is still in the noise. Should aircraft activity increase as projected, the global effects would become significant by 2050.

Acknowledgments. We are grateful to Drs. Michael King, Steven Platnick, Mark Gray, and David Starr. Thanks are given to Ellsworth Welton of NASA Goddard Space Flight Center, James Campbell of Science Systems and Application, Inc., at GSFC, Dr. Patrick Minnis of NASA Langley Research Center, Dr. Andrew Heymsfield of the National Center for Atmospheric Research, and Dr. Sergey Matrosov of the Cooperative Institute for Research in Environmental Sciences, University of Colorado, for supporting data and insightful discussions, and to William Cronin for assisting the angular calibration of the photographs. Ms. Tricia Gregory and Mr. Andrew Garcia of GSFC provided valuable miscellaneous assistance. Atlas is also appreciative of the continued hospitality of the NASA Goddard Space Flight Center. Doctor Wang is supported by the NASA CloudSat project and DOE Grant DE-FG02-03ER63536 from the Atmospheric Radiation

Measurement Program. Doctor Duda's participation is supported by the NASA Pathfinder Program and the NASA Office of Earth Science Radiation Sciences Program.

APPENDIX

List of Abbreviations Used in Table 1

TABLE A1. Airport identifier codes from Table 1.

Code	Airport name	Location
4R4	Fairhope Municipal (H. L. "Sonny" Callahan) Airport	Fairhope, AL
AGS	Augusta Regional Airport (at Bush Field)	Augusta, GA
AHN	Athens–Ben Epps Airport	Athens, GA
ATL	Hartsfield–Jackson Atlanta International Airport	Atlanta, GA
BDL	Bradley International Airport	Hartford, CT
BHM	Birmingham International Airport	Birmingham, AL
BOS	Logan International Airport	Boston, MA
CLT	Charlotte/Douglas International Airport	Charlotte, NC
CUN	Cancún International Airport	Cancún, Mexico
EDDL	Düsseldorf International Airport	Düsseldorf, Germany
EWR	Newark Liberty International Airport	Newark, NJ
HPN	Westchester County Airport	White Plains, NY
JFK	John F. Kennedy International Airport	New York, NY
LGA	La Guardia Airport	New York, NY
MCO	Orlando International Airport	Orlando, FL
MHT	Manchester International Airport	Manchester, NH
MSY	New Orleans International Airport	New Orleans, LA
PHL	Philadelphia International Airport	Philadelphia, PA
PIE	St. Petersburg/Clearwater International Airport	St. Petersburg, FL
PVD	T. F. Green International Airport	Providence, RI
TEB	Teterboro Airport	Teterboro, NJ
TPA	Tampa International Airport	Tampa Bay, FL

TABLE A2. Airline identifier codes from Table 1.

Code	Airline name
BTA	Express Airlines, Inc. (Continental Express)
COA	Continental Air Lines, Inc.
DAL	Delta Air Lines, Inc.
JBU	Jet Blue Airways Corporation
LTU	LTU International Airways
NNW	Private aircraft
NTF	Private aircraft
SNK	Sun Jet International, Inc. (Southeast Airlines)
SWA	Southwest Airlines Co.
USA	US Airways, Inc.

REFERENCES

Appleman, H., 1953: The formation of exhaust contrails by jet aircraft. *Bull. Amer. Meteor. Soc.,* **34,** 14–20.

Atlas, D., S. Y. Matrosov, A. J. Heymsfield, M.-D. Chou, and D. B. Wolff, 1995: Radar and radiation properties of ice clouds. *J. Appl. Meteor.,* **34,** 2329–2345.

Boin, K. V., and L. Levkov, 1994: Numerical simulation of the lifetime of contrails. *Impact of Emissions from Aircraft and Spacecraft upon the Atmosphere,* U. Schumann and D. Wurzel, Eds., DLR-Mitteilung, 430-435.

Brown, P. R. A., and P. N. Francis, 1995: Improved measurements of the ice water content in cirrus using a total-water probe. *J. Atmos. Oceanic Technol.,* **12,** 410–414.

DeGrand, J. Q., A. M. Carleton, D. J. Travis, and P. J. Lamb, 2000: A satellite-based climatic description of jet aircraft contrails and associations with atmospheric conditions. *J. Appl. Meteor.,* **39,** 1434–1459.

Douglas, R. H., K. L. S. Gunn, and J. S. Marshall, 1957: Pattern in the vertical of snow generation. *J. Meteor.,* **14,** 95–114.

Duda, D. P., P. Minnis, L. Nguyen, and R. Palikonda, 2004: A case study of the development of contrail clusters over the Great Lakes. *J. Atmos. Sci.,* **61,** 1132–1146.

Garber, D. P., P. Minnis, and P. K. Costulis, 2005: A commercial flight track database for upper tropospheric aircraft emission studies over the USA and southern Canada. *Meteor. Z.*, **14,** 445–452.

Gierens, K. M., 1996: Numerical simulations of persistent contrails. *J. Atmos. Sci.,* **53,** 3333–3348.

——, and E. Jensen, 1998: A numerical study of the contrail-to-cirrus transition. *Geophys. Res. Lett.,* **25,** 4341–4344.

Gunn, K. L. S., and J. S. Marshall, 1955: The effect of wind shear on falling precipitation. *J. Meteor.,* **12,** 339–349.

Heymsfield, A. J., 1975: Cirrus uncinus generating cells and the evolution of cirriform clouds. Part I: Aircraft observations of the growth of the ice phase. *J. Atmos. Sci.,* **32,** 799–808.

——, and R. M. Sabin, 1989: Cirrus crystal nucleation by homogenous freezing of solution droplets. *J. Atmos. Sci.,* **46,** 2252–2264.

——, R. P. Lawson, and G. W. Sachs, 1998: Growth of ice crystals in a precipitating contrail. *Geophys. Res. Lett.,* **25,** 1335–1338.

——, S. Matrosov, and B. Baum, 2003: The ice water path–optical depth relationships for cirrus and deep stratiform ice cloud layers. *J. Appl. Meteor.,* **42,** 1369–1390.

Jensen, E. J., A. Í. Ackerman, D. E. Stevens, O. B. Toon, and P. Minnis, 1998: Spreading and growth of contrails in a sheared environment. *J. Goephys. Res.,* **103** (D24), 31 557–31 567.

Khvorostyanov, V., and K. Sassen, 1998: Cloud model simulation of a contrail case study: Surface cooling against upper tropospheric warming. *Geophys. Res. Lett.,* **25,** 2145–2148.

Klett, J. D., 1981: Stable analytical inversion solution for processing lidar returns. *Appl. Opt.,* **20,** 211–220.

Knollenberg, R. G., 1972: Measurements of the growth of the ice budget in a persisting contrail. *J. Atmos. Sci.,* **29,** 1367–1374.

Konrad, T. G., and J. C. Howard, 1974: Multiple contrail streamers observed by radar. *J. Appl. Meteor.,* **13,** 563–572.

Lawson, R. P., A. J. Heymsfield, S. M. Aulenbach, and T. L. Jensen, 1998: Shapes, sizes, and light scattering properties of ice crystals in cirrus and a persistent contrail during SUCCESS. *Geophys. Res. Lett.,* **25,** 1331–1334.

Lewellen, D. C., and W. S. Lewellen, 2001: The effects of aircraft wake dynamics on contrail development. *J. Atmos. Sci.,* **58,** 390–406.

Matrosov, S. Y., A. V. Korolev, and A. J. Heymsfield, 2002: Profiling cloud ice mass and particle characteristic size from Doppler radar measurements. *J. Atmos. Oceanic Technol.,* **19,** 1003–1018.

Miloshevich, L. M., H. Vömel, A. Paakkunen, A. J. Heymsfield, and S. J. Oltmans, 2001: Characterization and correction of relative humidity measurements from Vaisala RS80-A radiosondes at cold temperatures. *J. Atmos. Oceanic Technol.,* **18,** 135–156.

Minnis, P., 2003: Contrails. *Encyclopedia of Atmospheric Sciences*, J. Holton, J. Pyle, and J. Curry, Eds., Academic Press, 509–520.

——, D. F. Young, D. P. Gardner, L. Nguyen, W. L. Smith Jr., and R. Palikonda, 1998: Transformation of contrails into cirrus during SUCCESS. *Geophys. Res. Lett.,* **25,** 1157–1160.

——, J. K. Ayers, R. Palikonda, and D. Phan, 2004: Contrails, cirrus trends, and climate. *J. Climate,* **17,** 1671–1685.

Palikonda, R., P. Minnis, P. K. Costulis, and D. P. Duda, 2002: Contrail climatology over the USA from MODIS and AVHRR data. *Proc. 10th Conf. on Aviation, Range, and Aerospace Meteorology*, Portland, OR, Amer. Meteor. Soc., J9–J12.

Ponater, M., S. Marquart, and R. Sausen, 2002: Contrails in a comprehensive global climate model: Parameterization and radiative forcing results. *J. Geophys. Res.,* **107,** 4164, doi:10.1029/2001JD000429.

Sassen, K., 1997: Contrail-cirrus and their potential for regional climate change. *Bull. Amer. Meteor. Soc.,* **78,** 1885–1903.

Schröder, F., and Coauthors, 2000: On the transition of contrails into cirrus clouds. *J. Atmos. Sci.,* **57,** 464–480.

Spinhirne, J. D., W. D. Hart, and D. P. Duda, 1998: Evolution of the morphology and microphysics of contrail cirrus from airborne remote sensing. *Geophys. Res. Lett.,* **25,** 1153–1156.

Stephens, G. L., and Coauthors, 2002: The CloudSat mission and the EOS constellation: A new dimension of space-based observations of clouds and precipitation. *Bull. Amer. Meteor. Soc.,* **83,** 1771–1790.

Uthe, E. E., N. B. Nielsen, and T. E. Osberg, 1998: Airborne scanning lidar observations of aircraft contrails and cirrus clouds during SUCCESS. *Geophys. Res. Lett.,* **25,** 1339–1342.

Whiteman, D. N., B. Demoz, and Z. Wang, 2004: Subtropical cirrus cloud extinction to backscatter ratios measured by Raman Lidar during CAMEX-3. *Geophys. Res. Lett.,* **31,** L12105, doi:10.1029/2004GL020003.

Winker, D. M., J. R. Pelon, and M. P. McCormick, 2003: The CALIPSO mission: Spaceborne lidar for observation of aerosols and clouds. *Lidar Remote Sensing for Industry and Environment Monitoring III.*, U. N. Singh, T. Itabe, and Z. Liu, Eds., International Society for Optical Engineering (SPIE Proceedings Vol. 4893), 1–11.